

**Metallic species, oxygen and silicon in the lunar exosphere: upper limits and prospects for LADEE measurements**

Menelaos Sarantos<sup>1, 2, 3,\*</sup>, Rosemary M. Killen<sup>4, 3</sup>, David A. Glenar<sup>5, 6, 3</sup>, Mehdi Benna<sup>7, 2</sup>, and Timothy J. Stubbs<sup>7, 2</sup>

(1) Heliophysics Science Division, NASA Goddard Space Flight Center, Greenbelt, MD, USA

(2) Goddard Earth Sciences and Technology Center, University of Maryland, Baltimore County, Baltimore, MD, USA

(3) NASA Lunar Science Institute, NASA Ames Research Center, Moffett Field, CA, USA

(4) Planetary Magnetospheres Branch, NASA Goddard Space Flight Center, Greenbelt, MD, USA

(5) Astronomy Department, New Mexico State University, Las Cruces, NM, USA

(6) Emeritus, NASA Goddard Space Flight Center, Greenbelt, MD, USA

(7) Solar System Exploration Division, NASA Goddard Space Flight Center, Greenbelt, MD, USA

\*corresponding author. Fax: +1 301 286 1648. Phone: +1 301 286 2945

*E-mail address:* menelaos.sarantos-1@nasa.gov

## **Abstract**

The only species that have been confirmed in the lunar exosphere are Na, K, Ar, and He. Models for the production and loss of lunar regolith-derived exospheric species from source processes including micrometeoroid impact vaporization, sputtering, and, for Na and K, photon-stimulated desorption, predict a host of other species should exist in the lunar exosphere. Assuming that loss processes are limited to ballistic escape and recycling to the surface, we have computed column abundances and compared them to published upper limits from the Moon and to detected abundances from Mercury. Only for Ca do the available measurements show a clear deficiency compared to the model estimates. This result suggests the importance of loss processes not included in the model, such as the possibility of gas-to-solid phase condensation during micrometeoroid impacts or the formation of stable metallic oxides, and underlines the need for improved spectroscopic measurements of the lunar exosphere. Simulations of the neutral mass (NMS) and visible/ultraviolet spectrometry (UVS) investigations planned by the Lunar Atmosphere and Dust Environment Explorer (LADEE) spacecraft are presented. Our calculations indicate that LADEE measurements promise to make definitive observations or set stringent upper limits for all regolith-driven exospheric species. Our models, along with LADEE observations, will constrain assumed model parameters for the Moon, such as sticking coefficients, source processes, and velocity distributions.

### *Keywords:*

Moon, Atmosphere

Moon, Surface

Atmospheres,

Structure

## 1. Introduction

Our Moon presents the nearest example of a common type of atmosphere, a *Surface Bounded Exosphere*. To date, only four constituents from this collisionless atmosphere have been positively identified: Ar and He, which were detected in situ by the neutral mass spectrometer deployed by Apollo 17, and Na and K, which have been extensively studied since their detection with ground-based telescopic observations in the late 1980s. (See Stern (1999) for a review of literature.) Many more species of regolith origin are expected to populate the lunar exosphere given the presence of neutrals such as O, Ca, and Mg in the similar exospheric environment of Mercury (e.g., Killen et al., 2007; McClintock et al., 2009). Hilchenbach et al. (1992) and Mall et al. (1998) measured pickup ions of lunar origin on early missions. More recently, lunar pickup ions such as  $\text{He}^+$ ,  $\text{C}^+$ ,  $\text{O}^+$ ,  $\text{Na}^+$ ,  $\text{K}^+$ , and  $\text{Ar}^+$  were observed above the Moon by the ion mass spectrometer onboard SELENE (Kaguya) (Yokota et al., 2009; Tanaka et al., 2009; Saito et al., 2010). It is unclear whether these ions are of exospheric origin or whether they are secondary ions sputtered directly from the surface (Elphic et al., 1991).

Searches have failed so far to detect other neutral elements mainly because, for many of the expected species, the strongest emission lines lie in the ultraviolet (UV) part of the spectrum. Nevertheless, published upper limits show clearly a non-stoichiometry, or disproportionality, between the exospheric and the surface abundances of numerous surface constituents (Fastie et al., 1973; Feldman and Morrison, 1991; Flynn and Stern, 1996; Stern et al., 1997). Alkalis are particularly enhanced in the exosphere. Possible

reasons for this trend are that Na and K are promoted to the gas phase through processes more efficient than other metals, that losses for other metals are more efficient than ballistic escape and photoionization would suggest, or both.

Regolith-derived atoms in the lunar exosphere, the focus of this paper, originate during the bombardment of the surface by solar photons, solar wind ions and micrometeoroids. These processes were reviewed for Mercury by Killen et al. (2007) and Domingue et al. (2007). For alkalis, such as sodium and potassium, the incident solar UV photons are energetic enough to break the sodium-regolith bonds and release atoms in a process termed photon-stimulated desorption (PSD) (Madey et al., 1998; Yakshinskiy and Madey, 1999). For refractory elements, which are tightly bound in silicate phases, only energetic processes such as high-speed impacts and sputtering by the solar wind can provide the energy needed to break those bonds. Consequently, the concentration of regolith-derived exospheric species reflects not only their relative surface abundance but also the micrometeoroid influx and speed, the amount of regolith vaporized, the sputtering yield per incident solar wind ion and the solar wind flux and composition, and other poorly constrained parameters. Loss processes also affect the exospheric content. For instance, many lunar and Hermean surface constituents may be promoted to the gas phase not only as atoms but also as molecular oxides (Killen et al., 2005; Killen et al., 2010; Berezhnoy and Klumov, 2008; Berezhnoy, 2010). If the dissociation lifetimes of such molecules as CaO, MgO, TiO, which are unknown, are long, the fraction of atomic neutrals that are bound in molecules will not be observed.

The interplay between source and loss processes must be constrained by models, improved exospheric observations, and laboratory experiments. In all three aspects,

sodium is by far the best studied species. Recently, Sarantos et al. (2010a) included results from twenty years of ground-based sodium exosphere observations, and compared the observed sodium intensity to the prevailing UV and solar wind environment during the time of the observation. Given PSD cross-sections somewhat smaller than laboratory-measured yields (Yakshinskiy and Madey, 1999) which do not account for loss inside the regolith (Cassidy and Johnson, 2007), the study found that sodium intensity levels closely matched the levels expected from models of the PSD process. However, when the Moon was in the solar wind (high ion flux environment), the exospheric sodium intensity levels typically increased by factors of 2-3 above the levels measured when the Moon was in the terrestrial magnetotail (low ion flux environment). The solar wind control of exospheric sodium could not be attributed to sputtering if sputtering yields typical of regolith surfaces,  $\sim 0.1$  atoms per ion impact, are assumed. It was concluded that the solar wind ions are augmenting the desorption process by enhancing the diffusion of sodium from regolith grains by up to a factor of two for fluxes typical of the solar wind in our immediate neighborhood, or increasing sodium levels by sputtering from multi-charged solar wind ions. Similar results are reported for Mercury's exospheric sodium in recent analyses of ground-based observations (e.g., Mura et al, 2009; Mouawad et al., 2011) and observations obtained by the MErcury Surface, Space ENvironment, GEochemistry, and Ranging (MESSENGER) spacecraft during three flybys (Burger et al., 2010). In summary, the sources that create the lunar sodium non-thermal population appear to be, in order of importance, photon-stimulated desorption (PSD), micrometeoroid impact vaporization, and solar wind sputtering.

The characterization of the Moon's exosphere with measurements from orbit is a

major science objective of the proposed Lunar Atmosphere and Dust Environment Explorer (LADEE) mission. LADEE will examine the lunar exosphere and dust environment with a payload consisting of a Neutral Mass Spectrometer (NMS), an Ultraviolet/Visible Spectrometer (UVS), and a Lunar Dust Experiment (LDEX). The nominal mission lifetime is planned to be 100 days sometime in 2013. The orbit is to be retrograde, equatorial, with periapse  $\sim 50$  km above the dawn terminator and an apoapse  $\sim 200$  km above the lunar dusk, although lower orbits ( $25 \times 75$  km) are being examined. The scientific objectives are to be achieved by measuring known species with spatial and temporal resolution sufficient to investigate the processes that control their distribution and variability, and by surveying a wide inventory of possible species to make new detections or to establish new upper limits (Delory et al., 2009).

To illuminate the existing measurements, help define expectations for the LADEE mission, and facilitate the interpretation of expected scientific results, we have carried out simulations of the production and loss of exospheric oxygen, silicon, and other metallic species. We have previously applied a model of exospheric particle transport to describe the source rates of the lunar sodium exosphere, and we validated it against ground-based observations (Sarantos et al., 2010). The model successfully described several key observables seen in sodium data: the overall emission rate, the subsolar density of  $\sim 60$ – $70$  atoms  $\text{cm}^{-3}$ , and an increase in scale height from the subsolar region to the terminator and poles. In Section 2 we extend this model to predict exospheric densities for O, Si, Fe, Al, Ti, Ca, Mg, K, and Mn. We compare the model to published upper limits, and we quantify the model uncertainties. In Section 3 we estimate what constraints LADEE NMS measurements can place on the generation of the lunar exosphere from these species. In

Section 4 we examine the expected levels of resonant scattering emission from these species, and assess whether their detection is affected by LADEE UVS instrument noise and zodiacal light. The paper concludes in Section 5 with a summary of our results, which show how LADEE measurements can further our present understanding: for many of the species studied and expected to be found, the expected signal-to-noise ratio will permit us to identify the processes and constrain the microphysical parameters (e.g., sputtering yields) controlling the supply of lunar gas and its interaction with the surface.

## 2. Exospheric abundances of species derived from the lunar surface

### 2.1 Model of particle transport

The production and distribution of lunar exospheric constituents is modeled with an analytical model of particle transport in a collision-free exosphere (Hartle, 1971). The model, which is a generalization of the Chamberlain (1963) model for non-uniform “exobase” density and temperature, uses Liouville’s theorem to compute the normalized density of neutrals,

$$n(\mathbf{r}) = \int f(\mathbf{r}, \mathbf{v}) d\mathbf{v} \quad (1)$$

given a truncated distribution function defined as:

$$f(\mathbf{r}, \mathbf{v}) = f_0(\mathbf{r} \rightarrow \mathbf{r}_0, \mathbf{v} \rightarrow \mathbf{v}_0) \times U(v_{r_0} > 0) \times \{1 - U(v_r < 0) \times U(v > v_{ESC})\} \quad (2)$$

where using the constants of motion under gravitational forces the velocity vector,  $\mathbf{v}$ , at a point,  $\mathbf{r}$ , in the exosphere is related to the point  $(\mathbf{r}_0, \mathbf{v}_0)$  of the surface where it originated;  $f_0(\mathbf{r}_0, \mathbf{v}_0)$  is the velocity distribution function of released particles from the surface; and



$U$  is a unit step function that delineates the populated region of phase space, i.e. the integration limits: (1) particles must originate from the surface with outward radial velocities,  $v_{r0} > 0$ , and (2) particles may not return ( $v_r < 0$ ) if they exceed escape velocity,  $v_{ESC}$ . It follows from Eq. 1 that the density anywhere in the exosphere can be computed with eqn. (2) provided that  $f_0$  is known (Section 2.1.1), and provided that the flux,  $n_0 \langle v_{r0} \rangle$ , is set to the surface source rate (Section 2.3).

### 2.1.1 Sources

Micrometeoroid impact vaporization and sputtering by solar wind ions are assumed to eject energetic atoms from the lunar surface. Additionally, UV photons acting upon the top monolayer of the surface can produce lower energy, but non-thermal, Na and K atoms. The atoms originate with initial speeds, bulk direction, and assumed variation in surface density that are characteristic of the source process, information that is captured in the assumed form of the distribution function of released atoms,  $f_0$ .

- For impact vaporization we assume a spatially uniform source of micrometeoroids that eject atoms with a Maxwellian distribution of upwards velocities from the surface:

$$f_0 = (m / 2\pi K_B T_0)^{3/2} e^{-\frac{m}{2K_B T_0} v_0^2} \quad (3)$$

where  $v_0$  the ejection speed,  $m$  is the mass of an atom for a relevant species, and  $K_B$  is the Boltzmann constant.

- For photon-stimulated desorption (PSD) we assume that the ejected atoms (Na and K) originate from the dayside having a Maxwellian velocity distribution and a dependence on solar zenith angle,  $\chi_0$  :

$$f_0 = (m / 2\pi K_B T_0)^{3/2} \cos \chi_0 e^{-\frac{m}{2K_B T_0} v_0^2} \quad (4)$$

- For sputtering the energy distribution,  $f$ , and directionality of the ejecta are described by the Sigmund-Thompson function :

$$f_0 = \frac{6 E_b}{3 - 8\sqrt{E_b / E_{Max}}} \frac{E_0}{(E_0 + E_b)^3} \{1 - \sqrt{(E_0 + E_b) / E_{Max}}\} \cos \delta_0 \quad (5)$$

where  $E_0$  is the ejected energy,  $E_b$  the binding energy of an atom to the surficial grain (e.g.,  $E_b = 2$  eV for sodium) and  $E_{Max}$  the maximum energy that can be imparted to the ejected surficial atoms by 1 keV solar wind protons that is typical at the Moon. (For the species studied here  $E_{Max}$  is typically a few hundred eV, but these velocities are highly improbable since  $f_0 \approx E_0^{-2}$  at high energies.) Due to the effects of soil porosity, the atoms are sputtered primarily perpendicular to the surface, with the yield assumed to reduce as the cosine of the angle,  $\delta_0$ , with respect to the local vertical direction.

### 2.1.2 Sinks

In our model only single hops are tracked, assuming that atoms that return to the surface adsorb, or stick, with unit efficiency and are not re-released. Losses to photoionization are insignificant on timescales of a single ballistic trajectory. Therefore, the modeled losses are ballistic escape and recycling to the surface. Although refractories

and K are expected to stick upon striking the surface, this is a poor assumption for Na for which tens of hops are likely prior to sticking because its sticking coefficient exhibits a strong temperature-dependence (Yakshinskiy and Madey, 2005). A partially thermalized sodium population due to energy exchange with the surface is excluded from our model. Because mainly high-altitude ( $\geq 100$  km) observations of the dayside were used for its validation (Sarantos et al., 2010), this model accurately predicts the observation above that altitude.

Other possible losses, most notably those relating to formation of molecular fragments and condensates, are neglected. Although relevant experiments are lacking, quenching theory predicts that gas condensation to solid grains in hypervelocity impacts may be an important loss process of impact-driven refractories (Berezhnoy and Klumov, 2008; Berezhnoy, 2010). For Ca we find clear evidence of losses that are not included in the model (Section 2.4).

## *2.2. Assumed surface composition*

Compositional estimates of the lunar surface are needed to initialize the model. Samples from four different types of soils have been brought back from the Moon: Highland, Kreep, low-Ti and high-Ti Mare soils (Wurz et al., 2007; Papike et al, 1982; Heiken et al., 1991). In broad terms, the elemental composition of Kreep and Mare soils is similar, whereas highlands have more Al and less Fe, Mg and Ti. The largest elemental variations across soil types are found for Ti (factor of ten more abundant in high-Ti Maria than in highlands), Fe (two to three times less abundant in highlands), and

K (three times more abundant in Kreep soils). These differences, summarized in Table 1, introduce the first of many uncertainties in our model estimates. For the estimates provided throughout this paper we assume a low-Ti Mare soil composition.

### 2.3. Estimated Source Rates

The vapor production rate by micrometeoroid impacts, which is a continuous source, was estimated using the model presented in Morgan and Killen (1997) and its subsequent improvements (Morgan and Killen, 1998; Killen et al., 2005). The model is based on the assumption that the delivery of meteoroid material at Earth's vicinity is at a rate of  $3 \times 10^{-16}$  g cm<sup>-3</sup> for particles smaller than 1 cm (Love and Brownlee, 1993); it is further assumed that the impact parameters of aluminum onto enstatite and the regolith porosity of 0.5 may be adopted. Letting impactors have speeds that exceed 5 km/s to vaporize refractories, the resulting total vaporization rate for all species at R = 1 AU is  $M_{\text{vap}} = 1.78 \times 10^{-16}$  g cm<sup>-2</sup> s<sup>-1</sup>. The vapor cloud was assumed to be stoichiometric,  $S_{IV} = c M_{\text{vap}} N_A / (\text{atomic weight})$ , where  $S_{IV}$  the production rate per species due to impact vaporization,  $c$  an elemental abundance in the soil, and  $N_A$  the Avogadro constant. Given a low-Ti Mare composition, impacts produce an estimated  $4 \times 10^6$  O atoms cm<sup>-2</sup> s<sup>-1</sup>. For a species like Mg we obtain  $2.5 \times 10^5$  Mg atoms cm<sup>-2</sup> s<sup>-1</sup>. The assumed temperature for this source process is T=3000 – 5000 K, close to the experimental values for hypervelocity impacts (e.g., Eichorn, 1978).

The production rate due to PSD may be estimated by assuming a sodium surface density  $\sigma \sim 3 \times 10^{12}$  cm<sup>-2</sup>, a flux  $F_{ph} \sim 2 \times 10^{14}$  cm<sup>-2</sup> s<sup>-1</sup> of UV photons ( $\geq 5$  eV) and an

effective PSD cross-section  $Q \sim 3 \times 10^{-21} \text{ cm}^2$  (Yakshinskiy and Madey, 1999). This results in a source rate,  $\sigma \times Q \times F_{\text{ph}}$ , of  $2 \times 10^6 \text{ atoms cm}^{-2} \text{ s}^{-1}$  at the subsolar point. This model setup was found to agree within a factor of two with the sodium ground-based observations (Sarantos et al., 2010). For potassium we assumed the same effective PSD yield as sodium. The inferred effective temperature from the laboratory experiments is  $T=1200 \text{ K}$  for this process.

The production rate due to ion sputtering was obtained by the following assumptions: a sputtering yield  $Y = 0.05$  per ion impact; a typical precipitating flux  $F_{\text{SW}} \approx 4 \times 10^8$  solar wind ions  $\text{cm}^{-2} \text{ s}^{-1}$ ; and the elemental number abundance,  $c$ , of a species of interest in the regolith (Table 1). These parameters yield a sputtered flux per species,  $S_{\text{SPUT}} = cY F_{\text{SW}}$ , that amounts to  $2.4 \times 10^7 \text{ O atoms cm}^{-2} \text{ s}^{-1}$  ( $2 \times 10^6 \text{ Mg atoms cm}^{-2} \text{ s}^{-1}$ ) at the subsolar point. At other solar zenith angles,  $\chi_0$ , this flux is assumed to reduce as  $\cos \chi_0$  due to the increased angle of solar wind incidence.

#### 2.4. Model results and comparisons with existing measurements

Model simulations of the expected release processes for several species are shown in Fig. 1. Within uncertainties in the micrometeoroid influx and the sputtering yield, impact vaporization and ion sputtering contribute equally to the release of gas over the subsolar region for fluxes typical of the solar wind at 1 AU. For exospheric refractories the two sources can be separately constrained in the vicinity of the Earth's magnetosphere by measuring the relative increase in exospheric levels when the Moon is exposed to the solar wind. Photon-stimulated desorption of Na and K much exceeds release of these two

species by impacts and sputtering as previously surmised (e.g., Sarantos et al., 2010). Estimated densities at LADEE altitudes from this model, shown in Fig.2, are small and generally less than the  $\sim 100$  atoms  $\text{cm}^{-3}$  predicted for O by the combined action of impacts and the solar wind. The gas densities could be even lower if formation of stable molecules and/or solids occurs.

Column abundances from the model are compiled in Table 2, along with available line-of-sight upper limits from the Moon (Stern, 1999). These were fitted to a Chamberlain (1963) model of uniform ejection at  $T=400$  K. The least stringent upper limit is that for lunar Mg because Hubble Space Telescope (HST) bright object avoidance constraints did not permit tangent heights any closer than 2,000 km from the surface (Stern et al., 1997). Also listed in Table 2 are detected abundances for known species at Mercury. Measurements of Ca, Mg, and Na over the southern pole at the time of MESSENGER's third flyby (Vervack et al., 2010) were fitted to Chamberlain models. Recent ground-based  $2\sigma$  detections of Mercury's Al and Fe are included (Bida and Killen, 2010). We do not include a putative detection of O from Mariner 10 data because scale heights were not reported.

The model predicted Na/K abundance ratio is four to five, in agreement with the  $6\pm 3$  Na/K abundance ratio obtained from observations (Potter and Morgan, 1988). The modeled column abundances for Fe and Mg are demonstrably below the upper limits, and those for Al and O approach limits. Modeled Si and Ti are four to six times above limits, but the transitions probed for these species from which the upper limits were derived are extremely unpopulated states (Section 4.1). We find only Ca to be unquestionably depleted. The deficiency of Ca most likely implies losses to condensation and molecular

formation not included in the model (Berezhnoy and Klumov, 2008; Berezhnoy, 2010). Notably, the Ca sputtered component alone also exceeds the observed limits. The mean solar wind flux on the day of that observation, July 30, 1994 (Flynn and Stern, 1996), was  $2.65 \times 10^8$  protons  $\text{cm}^{-2} \text{s}^{-1}$ , about half of what we assume in our baseline model, and the Moon was at quarter phase, clearly exposed to the solar wind. At these flux levels, the sputtered model would be consistent with the measurement if a sputtering yield no more than 0.01 ions/s were assumed.

In conclusion, the existing spectroscopic observations from the Moon show clear deviations from a stoichiometric model (impacts plus sputtering) only in the case of Ca, which may be ejected in molecular form. For other undetected species, including oxygen, modeled abundances are either clearly below published limits or do not differ significantly from measurements given uncertainties in surface soil abundance, micrometeoritic influx, and sputtering yields; their column ratios to Na and K can be explained by the effect of PSD, a process that is specific only to alkalis, and because Na does not stick to the surface upon impact. However, modeled Al and Fe at the Moon approach or exceed the levels recently detected at Mercury (Bida and Killen, 2010), but the Mercury observations were obtained at 1.5 Mercury radii from planetary center and necessarily represent the hot component. If the gases are indeed hot, other lunar refractory gases are likely to be below modeled levels. Improved spectroscopic observations closer to the planet are required to elucidate the production and loss of these undetected species of the lunar exosphere.

### *2.5. Model uncertainties*

Estimates of impact-driven production rates differ by roughly a factor of five because of uncertainties in the physical properties of the regolith and the impactors, the assumed micrometeoroid mass flux and velocity, and the method used to calculate the vapor yields (e.g., Cintala, 1992; Killen et al., 2005). Another estimate of the steady-state total vapor flux for all species at Earth's Moon is  $8.46 \times 10^{-17} \text{ g cm}^{-2} \text{ s}^{-1}$  compared to our rate,  $1.78 \times 10^{-16} \text{ g cm}^{-2} \text{ s}^{-1}$  (Bruno et al., 2006). Thus, our calculation agrees within a factor of two with other models. Our vapor predictions include the vapor produced by the volatilization of the impactors but exclude the possible enhancements of impact vapor produced during meteor showers.

The sputtering yields of neutrals are highly uncertain. We have assumed here a common sputtering yield of  $Y = 0.05$  atoms per incident ion for all species to establish a baseline model. This number is generally in agreement with results by Wurz et al. (2007), who included the mineralogy and solar wind energy dependence in TRIM simulations. Solar wind ions can sputter not only atoms but also ions from lunar soils. When bombarded with solar-wind-like 1–4 keV  $\text{H}^+$  and  $\text{He}^+$  ions, lunar soil simulants produced significant fluxes ( $\sim 10^3$ – $10^4$  ions  $\text{cm}^{-2} \text{ s}^{-1}$  per species) of secondary lunar ions (Elphic et al., 1991). In that experiment the flux of secondary ions was anticorrelated to ionization potential such that electronegative elements ( $\text{K}^+$ ,  $\text{Na}^+$ ,  $\text{Ca}^+$ ,  $\text{Al}^+$ ) had the highest ion yield. If so, then relatively smaller neutral sputtering yields should be expected for species such as K, Na, and Ca, and relatively higher sputtering yields may be expected for neutral O. More recently, experiments on sodium-bearing silicates demonstrated that almost all sputtered Na left the surface as ions, not as neutrals (Dukes et al., 2011). These results also revealed that large fractions of other sputtered species, like Al and Si, are sputtered



off primarily as ions. Last, it is unclear whether multiply charged solar wind ions may significantly enhance the yield from a planetary regolith surface (Shemansky, 2003; Meyer et al., 2011). Note the solar activity maximum conditions under which LADEE will operate.

The most significant uncertainties are losses to condensation and molecular formation during impacts. Molecules can be produced in the vapor + liquid + solid phase that follows micrometeoroid impact (Berezhnoy and Klumov, 2008; Berezhnoy, 2010) and, followed by dissociation, they can produce high-energy atoms of Mg, Ca, O, as well as other species. Mercury's high temperatures observed in the tail have been attributed to a dissociating molecule as the major source of energetic atomic Mg (Killen et al., 2010) and atomic Ca (Killen et al., 2005; McClintock et al., 2009). We know neither the abundance ratio of atoms versus molecules of the same species in the vapor cloud nor the molecular dissociation lifetime and temperature. Short,  $\leq 2$  min, molecule lifetimes and ratios of molecules-to-atoms of at least 4:1 are inferred from modeling of MESSENGER measurements of Mg (Sarantos et al., 2011). If stable gas molecules form, the local density of atomic elements driven by impacts is lower than the best-case estimates because a fraction of the molecule population returns to the surface before it is dissociated. If condensing, refractories condense in the following degree: Al and Ti > Ca > Si > Mg and Fe. According to quenching theory, the fraction remaining in the gas phase is  $\leq 1\%$  Al and  $\leq 5\%$  Ca at  $T \leq 4000$  K; at even lower temperatures,  $T = 3000$  K, Si < 1%, and Mg  $\sim$  Fe  $\sim 5\%$  in the gas phase (Berezhnoy, 2010). Na and K do not condense. Because of these possibilities (condensation plus molecular formation), the model abundances for refractory elements are probably upper limits as made clear for measured Ca.

### 3. Neutral Mass Spectroscopy

Although the primary goal of the neutral mass spectrometer onboard LADEE (LADEE NMS) is the detection of lunar volatiles, the instrument will search for the species studied here using its open source. The open source is designed specifically for surface-reactive species and has a relatively narrow field of view that excludes particles that map into the instrument with large entry angles relative to the its optical axis (Delory et al., 2009). The detection efficiency is also energy-dependent owing to the nature of the instrument's ion optics.

#### 3.1. Guiding Properties

To illustrate how the open source samples exospheric gases, Fig. 3 shows the populated portion of the velocity space in a Selenocentric system for Oxygen neutrals at the orbital altitude of 50 km above the subsolar point. We assume that these Oxygen neutrals originate from the lunar surface with three hypothetical distributions: (a) a Maxwellian at a temperature of 400 K that describes thermally accommodated ejecta, (b) a Maxwellian at a temperature of 3000 K that describes impact vaporization; and (c) a sputtering distribution. In the left hand column the two-dimensional distribution of local velocities is shown as a function of radial velocity,  $v_r$ , and the projection of the tangential component onto the plane of the orbit,  $v_\phi$ ; the distribution function is integrated for the out-of-the plane component. In the middle and right columns the three-dimensional distribution function for each of these sources is convolved with a proxy instrument

Wendy Barnes 7/19/11 2:31 PM  
**Comment:** Revise this figure here

response for different boresights. In this frame of reference the location of the spacecraft is denoted by the white dot. Solid white lines indicate the envelope of particle trajectories that connect to the surface, i.e. the limits of integration of Eq. 1. An instrument field of view of  $\pm 20^\circ$  is denoted by green dotted lines. Some of the specificities of mass spectrometers operating in an open source mode can be extracted from this figure:

- 1) For thermally accommodated neutrals (Fig 3A), the spacecraft “sits” outside the cloud of ejecta in inertial space, and the field of view of the open source encompasses a large fraction of the neutral distribution.
- 2) In contrast, for ejecta generated by impact vaporization and sputtering (Fig 3B and 3C), the open source captures only a small portion of the particle phase space.
- 3) For speeds typical of a lunar orbiter the counts are very sensitive to the instrument’s response at low energies. The dotted white circle around the spacecraft is the locus of neutral particles that arrive at the instrument with energy  $\leq 0.2$  eV; the dotted magenta circle encloses particles with energy  $\leq 0.5$  eV in the instrument’s reference frame. It is clear that in order for the mass spectrometer to detect exospheric particles from a  $T \leq 3000$  K source, the instrument energy cut-off should be lower than 0.5 eV.
- 4) The sensitivity is a function of pointing direction and temperature. As expected, for near-Maxwellian sources ram pointings are always preferable. For directional, high-energy sources, such as sputtering, very few particles arrive at the spacecraft with near-zero radial velocity. Therefore, pointings  $\geq \sim 30^\circ$  towards nadir would provide the best chance for detecting sputtered particles.

### 3.2 Model convolution for refractory species with the LADEE NMS response

In Fig. 4 a simplified proxy of the LADEE NMS “open source” response is convolved with the three-dimensional velocity distribution function to obtain counts per second for ram pointing as a function of spacecraft location and source temperature for a number of exospheric refractories. A nominal sensitivity of  $10^{-2}$  (counts/s) per (particle/cc) is assumed with a 0.2 eV energy cut-off (particles with energies lower than 0.2 eV will not be detected). The instrument sensitivity for some species may be better than assumed here due to their increased electron impact ionization cross-sections. We also assume a detector noise level of 0.01 counts/s

Assuming high-energy velocity distributions (left panel of Fig. 4), our calculations indicate that modeled O, Si (impacts) and Na (PSD) counts per second are near instrument noise levels, whereas other metallic species are undetectable. Assuming low-energy distributions (right panel of Fig 4), the maximum instrument counts per second were estimated using the upper limits summarized in Stern (1999) with  $T=400$  K. In that case, all species but Ti are detectable owing to the assumptions of higher local density and the greater fraction of phase space that NMS observes for low temperature sources. Note that models on the left and right are effectively equivalent in terms of column abundance (Table 2). Models on the left are “preferable” because an energetic parent process is required to initially vaporize refractories from the rock, but it is conceivable that returning gas particles might weakly adsorb and then thermally desorb around the subsolar point, thus providing a secondary source of ambient atoms (e.g., Hunten et al., 1988).

Should two populations be present, we quantify in Table 3 the fraction of local density seen by the instrument as a function of species mass and temperature, and estimate the minimum density that results in a signal-to-noise ratio of two. This was given assuming an optimal pointing direction (30 degrees towards nadir for sputtered species, and ram pointing for the rest). LADEE NMS can detect cold O down to  $\sim 36$  atoms  $\text{cm}^{-3}$  with its open source, which is more than an order of magnitude less than present limits, and can therefore irrefutably answer questions of whether oxygen is hot or not. No sputtered species can be detected at the assumed levels of instrument sensitivity because the very small fraction of phase space seen, 0.2–0.3 %, necessitates sputtered densities exceeding 1,000 atoms  $\text{cm}^{-3}$  for measurable counts. These results are obviously dependent on the assumed instrument cut-off energies and noise levels. The performance of the actual mass spectrometer will be measured during the instrument calibration. For completeness, we provide estimates for Sulfur, a species of meteoritic origin, that should be accessible for detection using the mass spectrometer's open source. With an upper limit of 150 S atoms  $\text{cm}^{-3}$  and the assumed temperature of 400 K (Stern, 1999), we predict  $\sim 1$  c/ 10 sec at a periapse of 25 km, which should be detectable.

#### 4. Ultraviolet-Visible Spectroscopy

##### 4.1 Main Emission Lines and $g$ -values in the UVS spectral range (230 – 825 nm)

$G$ -factors for the primary Na, K, Mg, and Ca lines were recently calculated for Mercury and were scaled to 1 AU (Killen et al., 2009). For other species of interest we assembled a table of ground states and calculated improved resonance scattering  $g$ -factors

metabolism-2015-01-22-31.pdf  
**Comment:** Rosemary, please add any comments you may have regarding your methodology here.

that include the effects of fluorescence (Table 4) (Chamberlain and Hunten, 1987, eqn. 6.2.4). High-resolution solar flux spectra were obtained from Kurucz, whereas the oscillator strengths were obtained from the NIST database (Ralchenko et al., 2010). These  $g$ -values are plotted in Fig. 5 as a function of an atom's radial velocity with respect to the Sun. Based on the requirements of ground state, high solar flux and oscillator strengths, and low instrument noise, the "optimal" target lines in the UVS spectral range, ~200 – 800 nm, are: Si (2515, 2517, 2529); Fe 2719; Al (3944, 3962); and Ti (3636, 3983, 3991, 3999).

The following findings must be noted:

- The  $g$ -value for Al 3092 is an order of magnitude less than the Morgan and Killen (1997) value. There is a deep solar line nearby and a high-resolution solar spectrum may not have been available at the time.
- The effect of fluorescence (pumping from other levels) is significant for Si (2515, 2519, 2529) and Al (3944, 3962) lines. Due to this effect the Al 3962 emission is twice that of Al 3944.
- The Al and Ti  $g$  values show a strong dependence on radial velocity. This result means that sputtered Al and Ti atoms (highly directional towards the Sun on the dayside) see a much larger portion of the solar continuum and will scatter light much more efficiently than impact-driven atoms from these species. This effect was not included in our baseline simulations (Sections 4.2 and 4.3), which all assumed a  $g$  value at zero Doppler shift.
- Oscillator strengths for Al I lines of Table 4 are only given a 50% accuracy in the NIST tables. The oscillator strengths for Si and Ti are only known to 25%

accuracy.

- The Si I line at 3906, on which the upper limit from Stern (1999) was based, originates at 1.9 eV above the ground state. It is not expected to be highly populated.
- Likewise, the Ti I 5036 line, monitored by Flynn and Stern (1996), is an excited state. Thus highly unlikely to be populated.

These findings suggest that the published upper limits for Ti and Si are questionable.

#### *4.2 Modeled line emission*

Given these  $g$ -values, we computed intensities of the strong emission lines from eight species of interest, within the range of UVS spectral coverage (230 -- 825 nm). Sightlines for these simulations lie in the equatorial plane and have low-altitude tangent heights (10–40 km). Fig. 6 shows the known species, Na and K, due to a PSD source. With anticipated emission of a few kilorayleighs in their main lines, the spatial distribution of Na and K can be clearly observed in the dayside. Hence, the LADEE measurements, in tandem with models, will constrain not only the source rates for these species, but also the energy exchange of exospheric particles with the surface: the sticking and the thermal accommodation coefficients.

Fig. 7 shows emission estimates from numerous undetected species at levels expected from impact vaporization and sputtering. Assumptions for impact vaporization are stated in Section 2.3, i.e. total impact vapor rate of  $1.78 \times 10^{-16} \text{ g cm}^{-2} \text{ s}^{-1}$ ,  $T=3000 \text{ K}$ , and no condensates or molecules for a "best case" estimate. For sputtering, the common sputter yield of 0.05 atom/ion and the solar wind flux of  $4 \times 10^8 \text{ ions cm}^{-2} \text{ s}^{-1}$  were

assumed. Furthermore, shown in the same figure is the intensity that is consistent with the published limits from Stern (1999) using the Chamberlain model of T=400 K. Also shown is the LADEE UVS instrument Noise Equivalent Radiance (NER), defined as the radiance of a source that would produce a signal-to-noise ratio of unity in a  $\tau=1$  sec integration time.

### 4.3. UVS spectral simulations

Limb measurements by LADEE UVS were simulated using the line intensity predictions shown in Fig. 7 along with the anticipated spectral performance of the UVS. The UVS instrument is a modified Czerny-Turner spectrometer built by Ocean Optics, Inc., and is nearly identical in design to the Visible Spectrometer (VSP) on the Lunar Crater Observation and Sensing Satellite (LCROSS) experiment. It functions as a fiber-coupled “point” spectrometer with approximately 1 deg field-of-view. Measurements of lamp emission lines during VSP ground calibration showed that spectral resolution ( $\lambda/\Delta\lambda$ ) decreased with wavelength, with average values for  $\Delta\lambda$  of 0.66, 0.98 and 1.03 nm at wavelengths of 500-600, 400-500 and 300-400 nm respectively (Ennico et al. 2010). To create each LADEE UVS simulation, monochromatic line radiances were smoothed by convolving with a Gaussian passband function using a wavelength dependent width that conforms to the VSP measurements. This was accomplished by performing the convolution using a deformed wavelength coordinate ( $\lambda'$ ) in which  $\Delta\lambda'$  is constant, and then remapping that result back into the original set of wavelength points. A variation of this approach was previously used by one of us in the characterization of electronically

**Comment:** Menelaos, I would omit this trace in Fig. 7. We can't directly compare line intensities (R) with NER (R nm<sup>-1</sup>), because the detection limit also depends on instrument spectral resolution, which is why we need to create a "Fig. 8". The numerical values in Fig. 7 happen to be pretty close, but this is only because the LADEE spectral sampling is "of order" 1 nm. I should probably try to incorporate NER in Fig. 8 -- maybe as a separate panel. Let me work on that. I moved this definition down to the next section.

menelaos@arizona.edu 7/13/13 2:23 PM  
**Comment:** Dave, please revise the description of your simulations here. I would particularly welcome a few references on how you modeled the assumed wavelength-dependent spectral resolution...



tunable filters (Georgiev et al., 2002). The blurred spectra were then resampled at 0.56 nm point spacing which matches the sampling during tests of the LADEE UVS Engineering and Test Unit (ETU). Next, Gaussian noise was added at the levels anticipated for UVS. The sensitivity of the UVS ETU has been measured using calibrated incandescent and UV lamp sources which agree remarkably well (within a few percent) within their region of spectral overlap, between 440 and 500 nm wavelength. Values of noise equivalent radiance (NER) between 40-45 Rayleigh  $\text{nm}^{-1}$  were measured between ~400 and 580 nm (we define NER as the radiance of a source that would produce a signal-to-noise ratio of unity in a 1 sec integration time). Minimum detectable radiance increases slowly in the UV to ~70 R  $\text{nm}^{-1}$  at 250 nm, although the UV source calibration loses accuracy shortward of ~300 nm. It likewise increases to a value of ~150 near the long wavelength limit of UVS coverage (830 nm). Simulations for longer integration times were created by coaddition, assuming that the noise follows Poisson statistics.

Line detection simulations are presented in Fig. 8 as a function of spacecraft location, assuming a constant tangent height of 10 km and 60 s integration. Each simulation also shows the line spectrum (shifted downward by 80 R  $\text{nm}^{-1}$  for clarity) as it would be observed without instrument noise. (XXX)

Olave Gienar 4/22/18 8:54 PM  
**Comment:** Menelaos, There should be a few more comments here describing the simulations. I'll leave a placeholder here since I haven't yet updated the plots.

As LADEE approaches orbital sunset, coronal-zodiacal light (CZL) becomes a significant excess brightness component, since the UVS line-of-sight is aft pointing and lies within a few degrees of the Sun. The brightness of CZL at UV-Vis wavelengths

close to the Sun has been quantitatively mapped from lunar orbit during Apollo 16 coronal photographic sequences (MacQueen et al. 1974) and later using calibrated measurements by the Clementine Star Tracker cameras (Hahn et al. 2002). Along the ecliptic equator, brightness diminishes with increasing solar elongation angle ( $\epsilon$ ) as

$$CZL = Const \epsilon^{-2.45 \pm 0.05} \quad (X)$$

which is valid between  $\sim 3$  degrees to at least 30 degrees in  $\epsilon$  (Hahn et al. 2002). The color of CZL is known from rocket borne photometry (Pitz et al. 1979) and photometric measurements made by the Helios spacecraft (see review by Leinert et al. 1998) and is mildly reddened relative to solar irradiance. Using Equation X, combined with the known spectral reflectivity of the Clementine Star Tracker camera (Hahn 2002) and CZL photometry, one can model (c.f. Stubbs et al. 2010) the spectral radiance of CZL as seen by the UVS, as we show in the last two panels of Fig. X, where solar elongation angle along the line-of-sight is 22 deg and 12 deg respectively. The CZL contribution by itself with instrument noise omitted is shown shifted upward by  $80 \text{ R nm}^{-1}$ . These comparisons show that CZL is a significant excess brightness component and strongly influences the detection of lines at small solar elongation angles, but it diminishes to less than the instrument noise at most spacecraft positions on the dayside, and UVS spectra can be coadded without such corrections (upper panels). It should be pointed out that Zodiacal light is not an intrinsic noise source, since it can be modeled and removed from the measurements, typically to a level smaller than the instrument noise.

At the levels predicted when the Moon is exposed to both micrometeoroids and the solar wind, detections are strictly controlled by the UVS characteristics (noise and

spectral resolution). For lines such as Al 3944, Al 3962, Ca 4227 that lie in the low-noise portion of the UVS range (>380 nm), emission of ~30 R is resolvable with minute-long exposures. The main lines of Si, Mg, and Fe may be more difficult to observe because of higher UVS noise levels assumed at small wavelengths. Our modeling suggests that, besides Na and K, short UVS exposures will most strongly constrain the production, loss and (possibly) spatial distribution of Al and Ca, which could be detectable over half the dayside with 100 sec integration. With  $\tau \approx 100$  s Si, Fe, Mg, and Ti may be detectable over a limited area of the dayside when the tangent point lies approximately over the subsolar point.

Finally, it is pertinent to ask: what if our exospheric abundances are overtly optimistic? An estimate of the signal-to-noise ratio, *SNR*, at different integration times,  $\tau$  (sec), may be obtained as  $SNR = \sqrt{\tau} \times (Line\_Intensity(R) / \Delta\lambda) / NER(1sec)$ , where  $\Delta\lambda$  is the UVS spectral resolution. Scaled-down versions of the impact models were used to compute the exposure time required to achieve a signal-to-noise ratio of four given the spectral resolution and the assumed NER at each line (Table 5). These conservative calculations, which are summarized in Fig. 9, prove that LADEE UVS can discover regolith-derived exospheric species at levels at least ten times less than our impact models suggest if spectra from the whole mission are coadded. Specifically, Ca can be easily detected at levels more than two orders of magnitude less than present limits. This approach identifies the lowest possible detection limits during the duration of the mission, and underlines the extent to which we can separately constrain contributions by impacts and sputtering by analyzing data obtained when the solar wind is shielded by Earth's magnetosphere. For this calculation science operations for 90 days with a 50%

Michelle Sarantos 3/15/12 10:01 AM  
**Comment:** This paragraph will be revised now that we have the improved noise levels

duty cycle for UVS were assumed.

## 5. Summary

A model that simulates the release processes of micrometeoroid impact vaporization, solar wind sputtering, and photon-stimulated desorption (for Na and K), was used to evaluate abundances for a number of exospheric species originating from the lunar regolith. Our simulations suggest the following:

- The observed non-stoichiometry of exospheric refractories compared to Na and K levels is mainly attributed to photon-stimulated desorption of alkalis, and possibly evidence that Na does not stick to the surface on impact.
- At present limits, Mg, Fe, O, and Al are much less than, or comparable to, the levels which the combined action of meteoroids and the solar wind can provide (Table 2).
- Modeled Si and Ti column abundances are four and six times, respectively, more than published limits, which may be related to our finding that the Si (3906) and Ti (5036) lines, probed from the ground by Flynn and Stern (1996), corresponded to excited states that are unlikely to be populated.
- Measured Ca (upper limit from the Moon; detected level from Mercury) shows clear deficiency from the modeled abundances, i.e. evidence of loss processes beyond those due to ballistic escape, adsorption, and photoionization. It is 40 times underabundant compared to the modeled levels due to impacts, implying losses to a stable molecule or its condensation from gas to solid states in the vapor cloud with efficiency exceeding 90% (Berezhnoy, 2010). Further, Ca is present at

quantities below those predicted by the sputtered component, implying the effective sputtering yield of 0.01 atoms per ion or less. Electronegative species such as Ca, Na, K, and Al may be sputtered off as ions at the expense of lower neutral sputtering yields (Elphic et al., 1991; Dukes et al., 2011). Isotopic ratios of Ca in lunar grains are inconsistent with sputtering (Kerridge and Kaplan, 1978).

- Although we cannot say precisely how exospheric source and loss rates vary from Moon to Mercury, comparison of lunar models to Mercury's recently detected Al and Fe implies that other exospheric refractories may be below modeled levels.

Using this model, we simulated LADEE measurements for these species with the expectation that deviations between the model and LADEE data will constrain microphysical parameters such as the assumed sputtering yields, the degree of formation of condensates and molecular constituents, and the energy exchange with the surface. At the levels predicted by our model, and assuming simplified instruments characteristics and performance, O and Si from nominal impact rates as well as Na from PSD should be at the NMS detectability level. If confirmed, this means that approximately a factor of three to four enhancements of impact vapor during meteor streams (for O and Si) and a factor of two enhancements during solar storms (for Na) should yield detectable signals if O and Si from impacts are coming off as atoms, and if the PSD efficiency for Na is enhanced by solar wind precipitation (e.g., Sarantos et al., 2010). The detection of possible colder ejecta is strictly controlled by the instrument sensitivity to incoming atoms in the 0.2–0.5 eV energy range. The actual energy characteristic of the instrument will be accessible during calibration. We finally predict that cold O at levels of 40 atoms

$\text{cm}^{-3}$  and S at levels of  $20 \text{ atoms cm}^{-3}$  can be detected with a signal-to-noise of two. Oxygen and sulphur can be constrained only by LADEE NMS because they emit outside the spectral range of the UVS.

Our simulations for LADEE UVS, based on the assumption of equatorial sightlines pointing aft and having low-altitude tangent points (10–40 km), demonstrate that Na and K will be observed throughout the dayside with high signal-to-noise ratio except near the terminator, where the contributions by dust scattering and Coronal-Zodiacal Light (CZL) dominate (Stubbs et al., 2010). The effect of ZL on line emission was shown to be negligible for spacecraft locations up to  $\pm 60^\circ$  from the subsolar point, therefore short exposures can be coadded without ZL removal over extensive regions of the dayside. Modeled spectra for other species in the UVS spectral range were convolved to UVS resolution with Gaussian noise added at about the level anticipated for UVS. At the levels predicted by impacts and sputtering, all species would be detectable with short, 100 s -5 min integrations over limited areas of the dayside. Given the unknown magnitude of sources and losses, lower column abundances were simulated in order to show that, if spectra from several dayside passes are coadded, Al, Ca, and Ti at surface densities exceeding  $0.02 \text{ atoms cm}^{-3}$ , and Si, Mg, and Fe at densities exceeding  $0.5 \text{ atoms cm}^{-3}$ , will be detectable with sufficient signal-to-noise ratio ( $S/N=4$ ). Detectable levels are one order of magnitude below published limits for Ti, more than two orders of magnitude below Ca limits, and at least one order of magnitude below nominal impact-driven models for other species (Table 2).

Acknowledgements: NSO/Kitt Peak FTS data used here were produced by NSF/NOAO.  $G_{\lambda}$  values were computed using the data in the NIST Atomic Spectra database online

[http://physics.nist.gov/PhysRefData/ASD/lines\\_form.html](http://physics.nist.gov/PhysRefData/ASD/lines_form.html) (Ralchenko et al., 2010).  
RMK acknowledges funding from the NASA Lunar Science Institute, DREAM.

## References

- Berezhnoy, A. A., 2010. Meteoroid bombardment as a source of the lunar exosphere, *Adv. Spa. Res.*, 45, 70–76.
- Berezhnoy, A. A., Klumov, B. A., 2008. Impacts as sources of the exosphere on Mercury. *Icarus*, 195, 511–522.
- Bida, T.A., Killen, R.M., 2010. Observations of the minor species Al, Fe, and Ca<sup>+</sup> in Mercury's exosphere, *Plan. Spa. Sci.*, submitted.
- Bruno, M., Cremonese, G., Marchi, S., 2006. Neutral sodium atoms release from the surface of the Moon induced by meteoroid impacts. *Mon Not R Astron Soc*, 367, 1067-1071.
- Burger, M.H., Killen, R.M., Vervack, R.J. Jr., Bradley, T.E., McClintock, W.E., Sarantos, M., Benna, M., Mouawad, N., 2010. Monte Carlo modeling of sodium in Mercury's exosphere during the first two MESSENGER flybys. *Icarus*, doi: 10.1016/j.icarus.2010.05.007, in press.
- Chamberlain, J. W., 1963. Planetary coronae and atmospheric evaporation. *Planet. Space Sci.*, 11, 901–960.
- Chamberlain, J.W. and D.M. Hunten, 1987. *Theory of Planetary Atmospheres*. Academic Press, New York, page 291.
- Cintala, M. E., 1992. Impact-induced thermal effects in the lunar and Mercurian regoliths. *J. Geophys. Res.*, 97, 947–973.
- Delory, G. T., Elphic, R., Morgan, T., Colaprete, T., Horanyi, M., Mahaffy, P., Hine, B., Boroson, D., 2009. The Lunar Atmosphere and Dust Environment Explorer



- (LADEE), 40th Lunar and Planetary Science Conference, (Lunar and Planetary Science XL), held March 23-27, 2009 in The Woodlands, Texas, id.2025.
- Dukes, C.A., W.Y. Chang, M. Famá, R. A. Baragiola, 2011. Laboratory studies on the sputtering contribution to the sodium atmospheres of Mercury and the Moon, *Icarus*, in press.
- Eichorn, G., 1978. Heating and vaporization during hypervelocity particle impact, *Plan. Spa. Sci.*, 26, 463-467.
- Elphic, R. C., H. O. Funsten, B. L. Barraclough, D. J. McComas, M. T. Paffet, D. T. Vaniman, and G. Heiken, 1991. Lunar surface composition and solar wind – induced secondary ion mass spectrometry, *Geophys. Res. Lett.*, 18, 2165–2168.
- Ennico, K., A. Colaprete, M. Shirley and D. Wooten, 2010. Lunar Crater Observation and Sensing Satellite (LCROSS) instrument calibration summary, V. 1, *LCROSS Instrument Summary for PDS*.
- Fastie, W. G., Feldman, P. D., Henry, R. C., Moos, H. W., Barth, C. A., Thomas, G. E., Donahue, T. M., 1973. A Search for Far-Ultraviolet Emissions from the Lunar Atmosphere. *Science*, 182, 710–711.
- Feldman, P. D., Morrison, D., 1991. The Apollo 17 Ultraviolet Spectrometer - Lunar atmosphere measurements revisited. *Geophys. Res. Lett.*, 18, 2105 – 2108.
- Flynn, B. C., Stern, S. A., 1996. A Spectroscopic Survey of Metallic Species Abundances in the Lunar Atmosphere. *Icarus*, 124, 530–536
- Georgiev, G., D. A. Glenar and J. J. Hillman, 2002. Spectral Characterization of Acousto-optic Filters Used in Imaging Spectroscopy, *Appl. Opt.*, 41, 209-217.

- Hahn, J.M., Zook, H.A., Cooper, B., Sunkara, B., 2002. Clementine observations of the zodiacal light and the dust content of the inner solar system. *Icarus*, 158, 360–378, doi:10.1006/icar.2002.6881.
- Hartle, R. E., 1971. Model for rotating and nonuniform planetary exospheres. *Phys. Fluids*, 14, 2592–2598.
- Heiken, G.H. D.T. Vaniman, and B.M. French, 1991. Lunar Sourcebook, Cambridge Univ. Press, New York, 736 pp.
- Hilchenbach, M., Hovestadt, D., Klecker, B., and Moebius, E., 1992. Detection of singly ionized energetic lunar pick-up ions upstream of earth's bow shock. In: Solar Wind Seven; Proceedings of the 3rd COSPAR Colloquium, Goslar, Germany, Sept. 16-20, 1991, 349-355.
- Killen, R. M., Bida, T.A., Morgan, T.H., 2005. The calcium exosphere of Mercury. *Icarus*, 173, 300–311.
- Killen, R. M., Cremonese, G., Lammer, H., Orsini, S., Potter, A.E., Sprague, A.L., Wurz, P., Khodachenko, M.L., Lichtenegger, H.I.M, Milillo, A., Mura, A., 2007. Processes that promote and deplete the atmosphere of Mercury. *Space Sci. Rev.*, 132, 433–509.
- Killen, R.M., Shemansky, D., Mouawad, N., 2009. Expected emission from Mercury's exospheric species, and their ultraviolet-visible signatures. *Astroph.J. Suppl. Ser.* 181, 351 – 359.
- Killen, R. M., Potter, A.E., Vervack, R.J., Jr., Bradley, E.T., McClintock, W.E., Anderson, C.M., 2010. Observations of metallic species in Mercury's exosphere. *Icarus*, doi :10.1016/j.icarus.2010.02.018, in press.

- Leinert, C., et al., 1998. The 1997 reference of diffuse sky brightness. *Astron. Astrophys. Suppl. Ser.*, 127, 1-99.
- Love, S.G., Brownlee, D.E., 1993. A direct measurement of the terrestrial mass accretion rate of cosmic dust. *Science*, 262, 550 – 553.
- Madey, T.E., Yakshinskiy, B.V., Ageev, V.N., Johnson, R.E., 1998. Desorption of alkali atoms and ions from oxide surfaces: relevance to origins of Na and K in the atmospheres of Mercury and the Moon. *Journ. Geophys. Res.*, 103, 5873 – 5887.
- Mall, U., Kirsch, E., Cierpka, K., Wilken, B., Söding, A., Neubauer, F., Gloeckler, G., and Galvin, A., 1998. Direct observation of lunar pick-up ions near the Moon, *Geophys. Res. Lett.*, 25, 3799-3802.
- MacQueen, R.M., Ross, C.L., Mattingly, T., 1973. Observations from space of the solar corona/inner zodiacal light. *Planet. Space Sci.* 21, 2173–2179.
- McClintock, W. E., Vervack, R.J. Jr., Bradley, E.T., Killen, R.M., Mouawad, N., Sprague, A.L., Burger, M.H., Solomon, S.C., Izenberg, N.R., 2009. MESSENGER observations of Mercury's exosphere: Detection of magnesium and distribution of constituents. *Science*, 324, 610–613.
- Meyer, F.W., P.R. Harris, C.N. Taylor, H.M. Meyer III, A.F. Barghouty, and J.H. Adams, Sputtering of lunar regolith simulants by protons and singly and multicharged Ar ions at solar wind energies. *Nucl. Inst. and Methods Phys. Res. B*, doi: 10.1016/j.nimb.2010.11.091, In press 2011.
- Morgan, T. H., Killen, R.M., 1997. A non-stoichiometric model of the composition of the atmospheres of Mercury and the Moon. *Planet. Space Sci.*, 45, 81–94.
- Morgan, T.H., Killen, R.M., 1998. Production mechanisms for faint but possibly detectable coronae about asteroids. *Planet. Space Sci.* 46, 843–850.
- Mouawad, N., Burger, M.H., Killen, R.M., Potter, A.E., Naidu, S., McClintock, W.E.,

- Vervack, R.J. Jr., Bardley, E.T., 2010. Constraints on Mercury's sodium exosphere: Combined MESSENGER and ground – based data. *Icarus*, submitted.
- Mura, A., P. Wurz, H. I. M. Lichtenegger, H. Schleicher, H. Lammer, D. Delcourt, A. Millilo, S. Orsini, S. Massetti, M. L. Khodachenko, 2009, The sodium exosphere of Mercury: Comparison between observations during Mercury's transit and model results, *Icarus*, **200**, 1-11.
- Pitz, E., Leinhart, C., Schulz, A., Link, H., 1979. Colour and polarization of the zodiacal light from the ultraviolet to the near infrared. *Astron. Astrophys.* 74 (1), 15–20.
- Potter, A.E., Morgan, T.H., 1988. Discovery of sodium and potassium vapor in the atmosphere of the Moon, *Science*, 241, 675–680.
- Ralchenko, Yu., Kramida, A.E., Reader, J. and NIST ASD Team, 2010. *NIST Atomic Spectra Database* (version 4.0), [Online]. Available: <http://physics.nist.gov/asd> [Wednesday, 08-Dec-2010 10:57:41 EST]. National Institute of Standards and Technology, Gaithersburg, MD
- Saito, Y., and 28 coauthors, 2010. In-flight Performance and Initial Results of Plasma Energy Angle and Composition Experiment (PACE) on SELENE (Kaguya). *Spa. Sci. Rev.*, 154, 265 – 303.
- Sarantos, M., Killen, R.M., Sharma, A.S., Slavin, J.A., 2010. Sources of sodium in the lunar exosphere: Modeling using ground-based observations and spacecraft data of the plasma. *Icarus*, 205, 364-374.
- Shemansky, D.E., 2003. The role of solar wind heavy ions in the space environment. AIP Conf. Proc. 663, Rarefied Gas Dynamics Intl Symposium Topics in Astrophysics 9, 687.
- Stern, S.A., 1999. The lunar atmosphere: history, status, current problems, and context,

- Rev. Geophys.*, 37, 453 – 491.
- Stern, S. A., Parker, J. W., Morgan, T. H., Flynn, B. C., Hunten, D. M.; Sprague, A., Mendillo, M., Festou, M. C., 1997. An HST Search for Magnesium in the Lunar Atmosphere. *Icarus*, 127, 523 – 526.
- Stubbs, T. J., Glenar, D. A., Colaprete, A., Richard, D. T., 2010. Optical scattering processes observed at the Moon: Predictions for the LADEE Ultraviolet Spectrometer. *Plan. Spa. Sci.*, 58, 830–837.
- Tanaka, T., and 12 coauthors, 2009. First in situ observation of the Moon-originating ions in the Earth's Magnetosphere by MAP-PACE on SELENE (KAGUYA), *Geoph. Res. Lett.*, 36, L22106, 10.1029/2009GL040682.
- Vervack, R.J. Jr., McClintock, W.E., Killen, R.M., Sprague, A.L., Anderson, B.J., Burger, M.H., Bradley, E.T., Mouawad, N., Solomon, S.C., Izenberg, N.R., 2010. Mercury's Complex Exosphere: Results from MESSENGER's Third Flyby. *Science*, doi: 10.1126/science.1188572, in press.
- Wurz, P., Rohner, U., Whitby, J.A., Kolb, C., Lammer, H., Dobnikar, P., Martín-Fernández, J.A., 2007. The lunar exosphere: The sputtering contribution, *Icarus*, doi:10.1016/j.icarus.2007.04.034.
- Yakshinskiy, B. V., Madey, T.E., 1999. Photon-stimulated desorption as a substantial source of sodium in the lunar atmosphere. *Nature*, 400, 642 – 644.
- Yakshinskiy, B. V., Madey, T.E., 2005. Temperature\_dependent DIET of alkalis from SiO<sub>2</sub> films: Comparison with a lunar sample. *Surf. Sci.*, 593, 202–209.
- Yokota, S., et al. , 2009. First direct detection of ions originating from the Moon by MAP-PACE IMA onboard SELENE (KAGUYA), *Geophys. Res. Lett.*, 36, L11201,

doi:10.1029/2009GL038185.

Table 1. Assumed composition of the lunar regolith (Low-Ti Mare soils) and variation across soil types (% relative abundance by number)

<i>Element</i>	<i>Low-Ti Mare soils</i>	<i>High-Ti Mare soils</i>	<i>Highland soils</i>	<i>Kreep soils</i>
O	60.26	60.30	60.82	60.47
Si	17.30	15.86	16.31	17.35
Al	5.56	5.70	10.66	6.48
Mg	5.53	5.70	3.84	5.39
Ca	4.44	4.60	5.92	4.43
Fe	5.85	5.29	1.90	4.47
Ti	0.66	2.01	0.17	0.62
Na	0.26	0.31	0.29	0.44
K	0.06	0.05	0.05	0.19
Mn	0.08	0.07	0.03	0.06

Notes: Averages taken from Wurz et al. (2007); Original data from Papike et al. (1982)

Table 2. Modeled Zenith Column Abundances are compared to known upper limits at the Moon and to known detections at Mercury

		<b>Moon</b>		<b>Mercury</b>		
Model (a)		Detections <sup>(b)</sup> or Upper Limits <sup>(c)</sup>		Detections <sup>(d),(e)</sup>		
	no (cm <sup>-3</sup> )	Zen.Col. Abundance (cm <sup>-2</sup> )	no (cm <sup>-3</sup> )	Zen.Col. Abundance (cm <sup>-2</sup> )	no (cm <sup>-3</sup> )	Zen.Col. Abundance (cm <sup>-2</sup> )
Na	70	1.9E09	67±12	8±3E08	872	1.4E10
K	14	3.5E08	15±3	1.4±0.3E08	308	2.1E09
Mg	5.5	4.4E08	≤ 6,000	≤ 5.4E10	13	1.4E09
Ca	3.6	2.0E08	≤ 1	≤ 5.0E06	0.5	3.9E07
Al	3.6	2.0E08	≤ 55	≤ 4.3E08	1	5.9E07
Fe	4.1	1.6E08	≤ 380	≤ 1.3E09	2	1.1E08
Ti	0.5	2.3E07	≤ 1	≤ 4.0E06	-	-
Si	16.3	1.2E09	≤ 48	≤ 3.6E08	-	-
O	66.3	6.2E09	≤ 500	≤ 7.4E09	-	-

(a) Modeled lunar Na and K attributed to PSD, other species attributed to impact vaporization

- (b) Lunar Na and K abundances are from the discovery measurements of Potter and Morgan (1988)
- (c) Lunar upper limits are Chamberlain fits to  $T = 400$  K (Stern, 1999)
- (d) Hermean Na, Mg, and Ca: Fits of a Chamberlain model to MESSENGER third flyby data over Mercury's southern hemisphere ( $T_{\text{Na}}=1,500$  K;  $T_{\text{Mg}}=20,000$  K;  $T_{\text{Ca}}=10,000$  K) (adapted from Vervack et al., 2010).
- (e) Hermean Al and Fe: Fits of a Chamberlain model to ground-based detections at respective temperatures of  $T_{\text{Al}}=3,000-9,000$  K and  $T_{\text{Fe}}=10,000$  K (Bida and Killen, 2010)

Table 3. Fraction of phase space seen by the open source LADEE NMS as a function of assumed source temperature

<i>Element</i>	<i>Fraction Observed (%)</i>	<i>Density (<math>\text{cm}^{-3}</math>) corresponding to <math>S/N = 2</math></i>	<i>Density (<math>\text{cm}^{-3}</math>) at periapse alt=25 km</i>
Hot O (3000 K)	1.0	200	63
Cold O ( 400 K)	5.5	36	412
Hot Si (3000 K)	1.6	125	15
Cold Si ( 400K)	10.0	20	34
Hot Na (1200 K)	2.4	83	50
Sputtered O	0.2	1,000	14

*Notes:* The density corresponding to  $S/N=2$  was calculated assuming NMS Sensitivity= $0.01$  (cts/s)/(atoms/ $\text{cm}^3$ ) and Noise =  $0.01$  cts/s;  
 No transmission of neutrals entering the instrument with  $E \leq 0.2$  eV is assumed;  
 Na is shown over the subsolar point (altitude = 50 km);  
 Sputtering computed for pointing= $30^\circ$  towards nadir; Else, ram pointing is shown;  
 "Cold" Si and O are computed from upper limits (Stern, 1999);  
 "Hot" Si and O are computed from impact vaporization model; "Hot" Na from PSD model



Table 4. Strongest emission lines of regolith-derived exospheric species in the LADEE  
UVS range (2316-8259 Å)

Species	wavelength vac (Å)	wavelength air (Å)	Ei	<i>g</i> _value
Fe I	2523.608	2522.849	0	4.0E-03 (old:0.03736)
Fe I	2719.833	2719.027	0	7.7E-03
Fe I	3720.99	3719.935	0	6.76E-03
Fe I	3859			4.57E-03
Al I	3083.048	3082.1529	0	4.87E-03
Al I	3093.6078	3092.7099	112.061	4.68E-03
Al I	3945.1222	3844.0058	0	1.83E-02 (old:0.0285)
Al I	3962.641	3961.520	112.061	3.64E-02 (old:0.0230)
Si I	2507.66	2506.90	77.115	1.66E-03
Si I	2515.08	2514.32	0	2.1E-03 (old: 0.028)
Si I	2516.87	2516.11	223.157	2.4E-03
Si I	2519.96	2519.2	77.115	1.58E-03
Si I	2524.87	2524.1	77.115	1.34E-03
Si I	2529.27	2528.5	223.157	2.60E-03
Ti I	3187.37	3186.451	0	2.95E-02
Ti I	3192.92	3191.99	170.132	2.10E-02
Ti I	3342.84	3341.88	0	2.06E-02
Ti I	3371.41	3370.44	0	2.2 E-02
Ti I	3636.50	3635.46	0	8.73E-02
Ti I	3643.72	3642.68	170.13	5.61 E-02
Ti I	3948.90	3947.77	170.13	
Ti I	3949.79	3948.67	0	5.62E-02
Ti I	3957.46	3956.34	170.13	4.1E-02
Ti I	3959.33	3958.21	386.87	6.0E-02
Ti I	3982.89	3981.76	0	6.78E-02
Ti I	3983.61	3982.48	0	1.80E-02
Ti I	3990.89	3989.76	170.13	6.92E-02
Ti I	3999.77	3998.64	386.87	6.87E-02
Mg I	2852.96	2852.127	0	3.2E-02
Ca I	4226.73	4227.92	0	4.9E-01
Na I	3303.32	3302.37	0	5.41E-04
Na I	3303.93	3302.97	0	5.85E-04

**Comment:** Rosemary, please fill in the missing fields

Na I	5891.6	5889.95	0	5.25E-01
Na I	5897.6	5895.92	0	3.07E-01
K I	4045.2	4044.136	0	3.1E-02
K I	4048.4	4047.28	0	1.26E-02
K I	7667.01	7664.89	0	2.76E0
K I	7701.08	7698.96	0	1.94E0
Mn I	2795.64	2794.82	0	2.8E-02
Mn I	2799.09	2798.27	0	2.17E-02
Mn I	2801.89	2801.06	0	1.5E-02
Mn I	4031.90	4030.76	0	1.5E-02
Mn I	4034.21	4033.07	0	1.09E-2
Mn I	4035.63	4034.49	0	7.64E-03

Notes: Listed are g-values at zero Doppler shift.

Table 5. LADEE UVS spectral parameters that were assumed in our simulations

Line	NER ( $R \text{ nm}^{-1}$ )	(nm)
Si 2515	285	1.27
Fe 2719	249	1.21
Mg 2852	226	1.16
Ti 3636	97	0.82
Al 3944	49	0.72
Ca 4227	43	0.70

**Comment:** Menelaos. I looked back at some notes from a dialogue with Rosemary a couple of years ago, when Tim & I were adding lines to our sim code. This is the K "D1" line ( $4^2P_{1/2} \rightarrow 4^2S_{1/2}$ ), but there is also the K "D2" line ( $4^2P_{3/2} \rightarrow 4^2S_{1/2}$ ) with vacuum wavelength  $\sim 7667.0$ . This coincides with a telluric O2 line (unless there's a large Doppler shift) so it's usually not reported in ground-based lunar obs. For D1, I had the same g-factor value as your table (g=1.7) which I got from Chamberlain '78. I tried to bootstrap a value for D2 (from D1) by ratioing line-center cross-sections (Sprague et al., Sci. '90, end-notes) and central intensities in the Fraunhofer lines. I got something like 2.8, but I'm not sure I did it correctly - I think Rosemary pointed out an error. In any case it's bright. Why not include that line in your table?

**Comment:** We will revise given Tony's new input

## Figure Captions

**Figure 1.** Model predictions of lunar exospheric refractories over the subsolar point.

**Figure 2.** Dayside exospheric density along a LADEE equatorial orbit (50×200 km) from impact vaporization, sputtering, and photon-stimulated desorption (for Na and K).

**Figure 3.** (Left column) Velocity distribution of lunar exospheric particles in the equatorial plane . (a) Oxygen accommodated to the local surface temperature; (b) Oxygen from micrometeoroid impact vaporization; (c) Oxygen from sputtering. (Middle and right columns), The relative fraction of neutrals mapping into the open source LADEE NMS (white dot) is shown for ram (0°) and off-ram pointings. Dotted green lines indicate the instrument’s effective field of view. Dotted white (magenta) circles centered on the spacecraft indicate the fraction of planetary neutrals not measured when an instrument potential of 0.2 V (0.5 V) is applied to suppress spacecraft outgassing.

**Figure 4.** Estimated c/s from the convolution of a LADEE NMS proxy response with (a) modeled three-dimensional distributions from micrometeoroid impact vaporization (MIV) and photon-stimulated desorption (PSD); and (b) modeled upper limits (Stern, 1999) which implicitly assume the accommodation of lunar exospheric particles to the surface temperature ( $T=400$  K). Models on the left and right are equivalent in terms of total column abundance (Table 2). “Detectability” is taken to be the level of instrument noise. The calculations exclude particles which arrive into the instrument with  $E \leq 0.2$  eV, whereas effects of the ionizing source, which may prevent the detection of particles with  $E \leq 0.5$  eV in some mass channels, are not included.

**Figure 5.**  $g$  values at  $r = 1$  AU are shown as a function of an atom’s velocity (with respect to the Sun) for the main lines of regolith-derived constituents of the lunar exosphere. For Mg, Ca, K, and Na lines see Killen et al. (2009).

**Fig. 6** Modeled intensity for Na and K from a PSD source for equatorial lines of sight

pointing from the spacecraft to the constant tangent altitude of 10 (red) and 40 km (blue).

**Figure 7** The modeled intensity from impact vaporization (red) and sputtering (green) for Si, Al, Mg, Fe, Ti, and Ca is compared to published upper limits (Stern, 1999). Also shown is the LADEE UVS instrument noise equivalent (NER) for 1-sec exposure (blue).

**Comment:** I would omit this trace in Fig. 7. (See my comment at the end of Secc 4.2)

**Figure 8** UVS simulations of spectral emission lines between 240-440 nm, following the LADEE orbit when the Moon is simultaneously exposed to micrometeoroids and the solar wind (predictions in Fig. 7). Integration time = 60 sec. These simulations are produced by spectrally convolving with a gaussian blur function that has a wavelength dependent width, as described in the text. Instrument noise is determined from measurements of the LADEE UVS Engineering and Test Unit (ETU). Noise free spectra are located below each simulation. Several species (e.g., Si, Al, Ca Na) should be detectable by UVS and thus spatially resolvable at this integration time. Coronal-zodiacal-light (CZL) is included in these simulations, but it contributes significantly only at longer wavelengths and small solar elongation angles, as shown by noise-free CZL models which are superimposed (offset) at the last two orbital positions.

**Fig. 9** Estimated exposure time as a function of assumed surface abundance to achieve a UVS signal-to-noise ratio (S/N) of four.. Levels at least ten times less than our impact model abundances, and at least one hundred times less than present limits for Ca, can be detected over the lifetime of the LADEE mission (90 days).

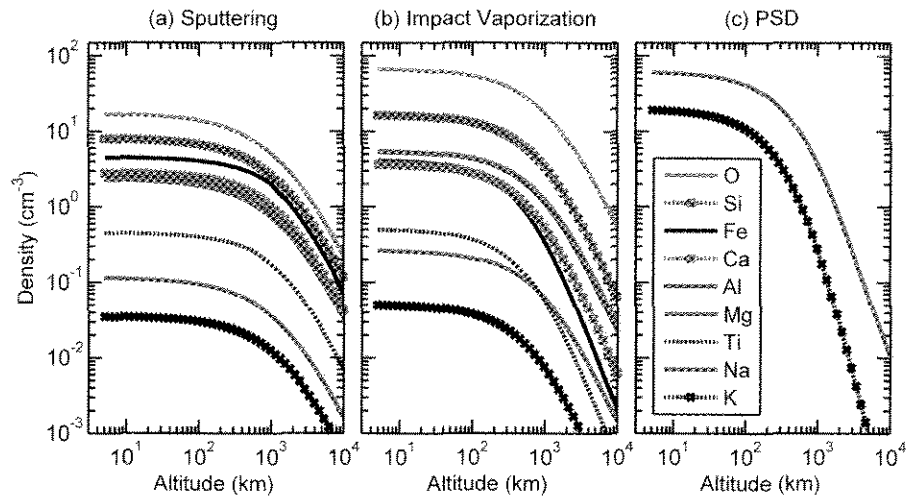


Figure 1

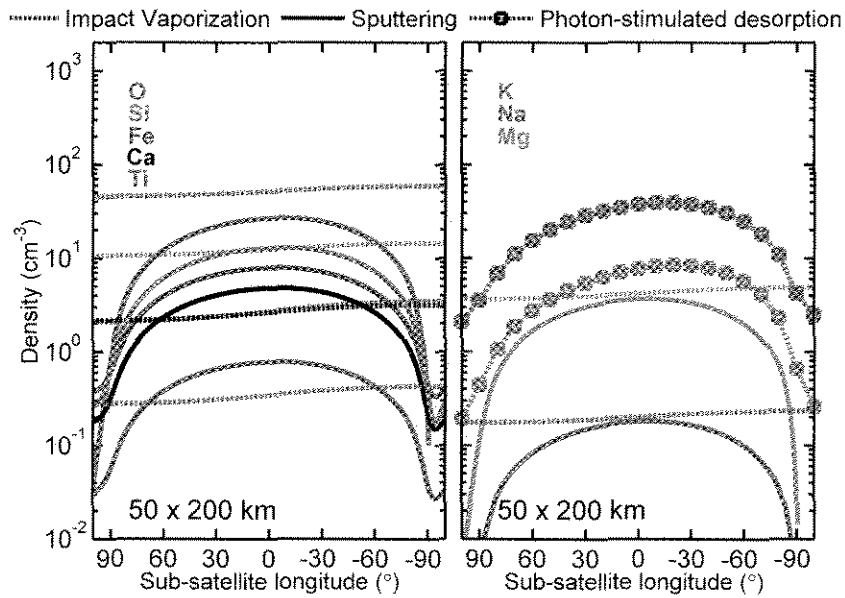


Figure 2

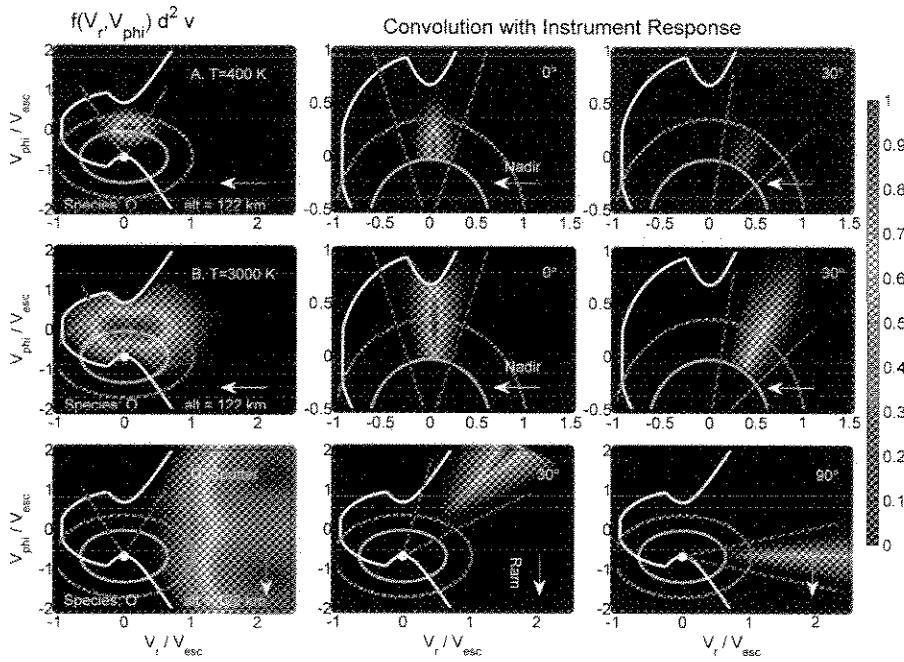


Figure 3

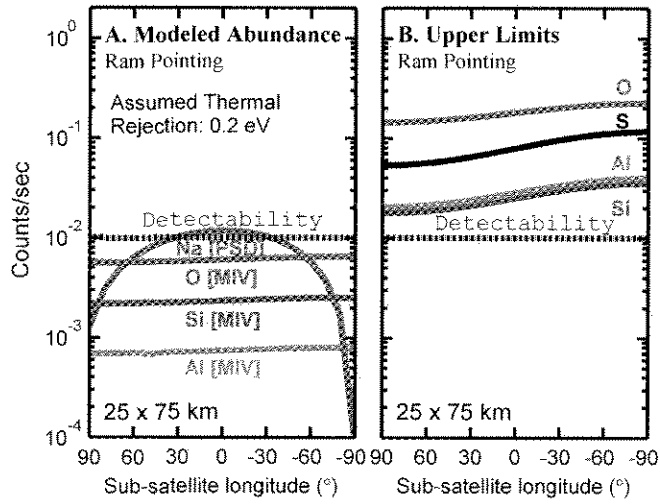


Figure 4

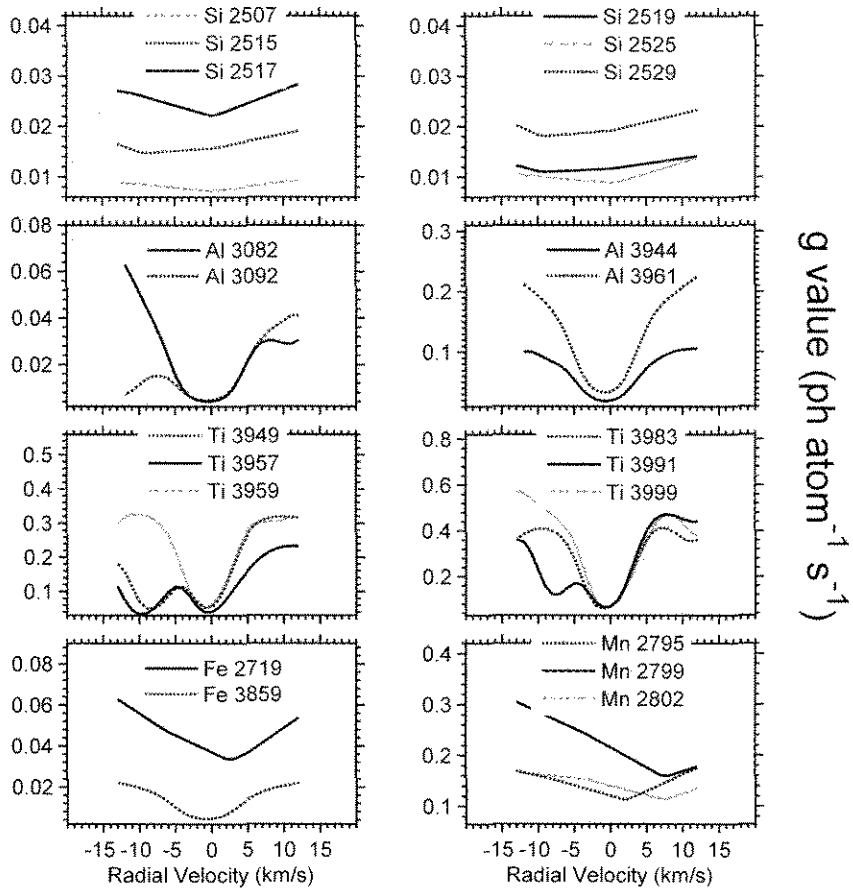


Figure 5:

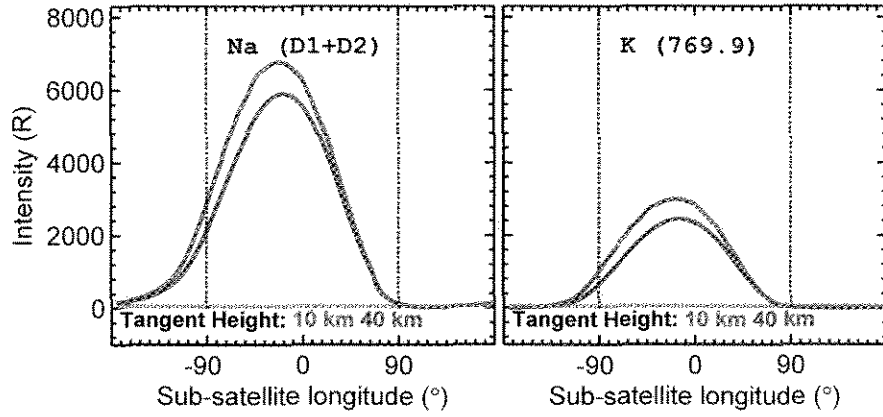


Figure 6

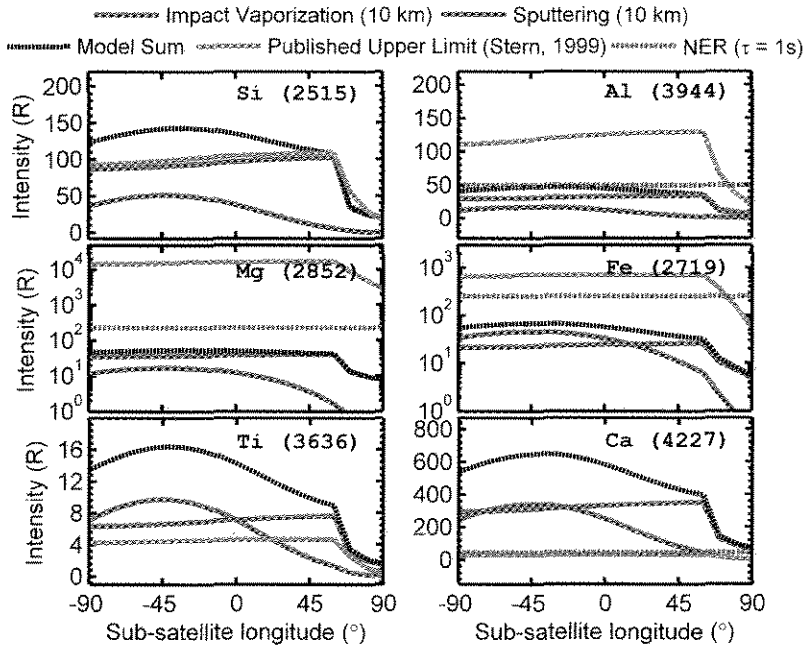


Figure 7



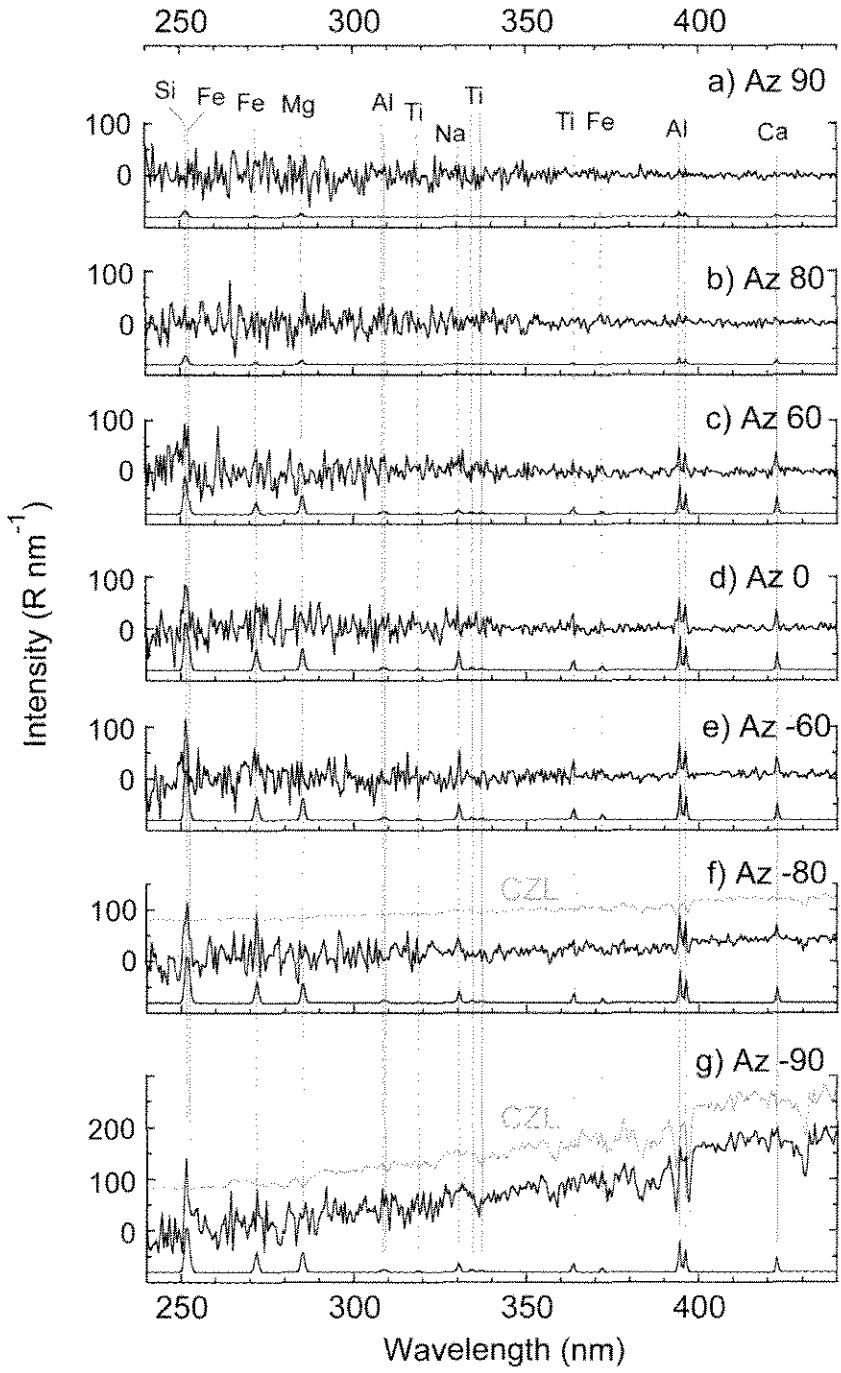


Figure 8

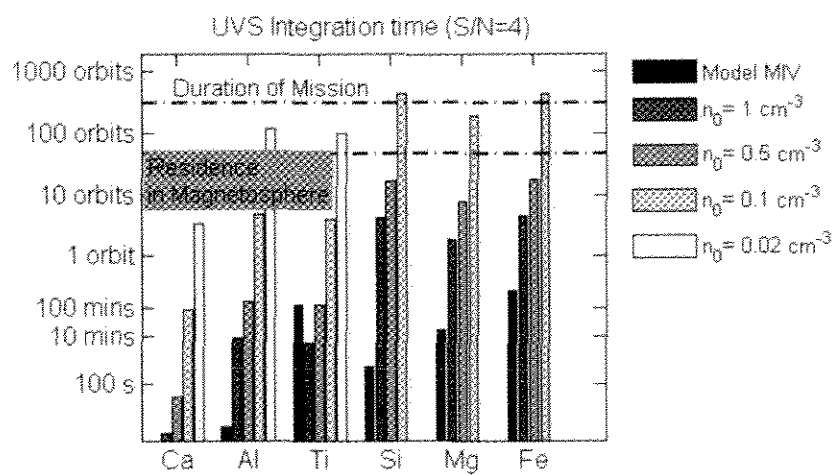


Figure 9